Dynamic Response Characteristics of Steep Loess Slope with a Tunnel under the Earthquake Actions

Jianping Yue , Qingguo Liang * , Chuntan Fan , Shijiu Li , Lili Wang , Weiyu Sun

Posted Date: 18 September 2023

doi: 10.20944/preprints202309.1122.v1

Keywords: Dynamic response characteristics; Damage evolution; Tunnel portal slope; Shaking table tests; Numerical simulations

Article

Dynamic Response Characteristics of Steep Loess Slope with a Tunnel under the Earthquake Actions

Jianping Yue [1,2], Qingguo Liang [1,*], Chuntan Fan [1], Shijiu Li [1], Lili Wang [3] and Weiyu Sun [1]

[1] School of Civil Engineering, Lanzhou Jiaotong University, Lanzhou, 730070, China
[2] School of Civil Engineering, Hexi University, Zhangye, 734000, China
[3] Key Laboratory of Loess Earthquake Engineering, Lanzhou Institute of Seismology, CEA, Lanzhou 730070, Gansu, China
* Correspondence: lqg_39@163.com

Abstract: With more and more transportation tunnels have been and will be constructed in loess areas in Northwest China with high earthquake potential, the overall stability of portal section under earthquakes actions and the related aseismic countermeasures attracted the attentions from both the scholars and engineers, especially the tunnels in the upper slope connecting the high bridges crossing rivers or valleys. In order to study the dynamic response characteristics and damage evolution of steep loess slope with a tunnel under the earthquake actions, a large-scale shaking table tests were performed on steep loess slope with a tunnel. Wenchuan-tangyu (WT) wave and El Centro (El) wave records were applied on the model to investigate the displacement response and acceleration response of loess slope with a tunnel under the horizontal (X) and the combined action of horizontal and vertical (X-Z) seismic loads, respectively. In particular, three-dimensional non-contact optical measurement techniques were used to obtain the slope surface displacements. The results showed that the main deformation pattern of the slope was horizontal movement and settlement when the seismic wave input was in the X and X-Z directions, respectively. However, the X direction seismic wave had a greater impact on the deformation of the slope, and the tunnel portal slope was destroyed under the action of a large horizontal seismic acceleration finally. Slope failure ahead of a tunnel could be divided into four stages, i.e. elastic deformation stage, plastic deformation accumulation stage, local failure stage, and overall failure stage. The peak ground displacement of X direction (PGD_X) and peak ground displacement of Z direction (PGD_Z) of the slope surface increased with the increasing of the input peak ground acceleration (PGA) when the input wave was same waveform and same direction. The existence of the tunnel had a great influence on the PGA and the PGA amplification factor (PGAAF) of the soil mass surrounding it. This was because the seismic waves encounter a tunnel surface with clear differences in the physical properties of the medium during their propagation in the slope, thereby forming a strong reflection and refraction effect, and the amplitude changed significantly. Numerical simulation results were basically consistent with the experimental results.

Keywords: dynamic response characteristics; damage evolution; tunnel portal slope; shaking table tests; numerical simulations

1. Introduction

In China, the distribution area of loess is 63.5×10^4 km^2, which is main in Gansu, Shaanxi, Ningxia, Shanxi, Henan and Qinghai, comprising the mainly body of the Loess Plateau [1]. The loess has a unique macropore and weak intergranular cementation structure in northwest of China [2]. The structure of the overhead pore form by the overlapping large solid particles which belong to the metastable structure system. The overlapping particles are main connected by the contacting of the tip of particles, resulting in low dynamic strength, which make them vulnerable to earthquakes [3]. The Loess Plateau is located in the areas of high seismic regions and high earthquake intensity. The area with PGA > 0.2g accounted for 26% of the total areas, while areas with PGA>0.15g account for 54%, with frequent moderately strong earthquake [3], which often cause cracking, deformation, instability, failure of loess slope, and induce geological hazards. The main inducing factors of loess

Preprints (www.preprints.org) | NOT PEER-REVIEWED | Posted: 18 September 2023 doi:10.20944/preprints202309.1122.v1

slope instability and failure are rainfall and earthquake, as shown in Figure 1. Generally speaking, rainfall-triggered landslides are mainly surface-level soil landslides (Figure 1a,b,d,e) [4]. Strength of the loess is greatly reduced, due to the original structure of loess particles is destroyed with the change of the water content [3]. Whereas, the mechanical effect of earthquakes on loess slopes is mainly reflected the triggering effect and in the superimposed effect. The superimposed effect induces progressive failure of the loess slope, and the triggering effect leads to the reduction of structural potential at weak structurally of the loess slope [5]. The influence of the earthquake on the soil, resulting the loss of cementation between the particles in the loess and the disintegration of the aggregates, and which lead to the damage of the loess structure and the decrease of the strength. The cracks may be first formed at the position where the disturbance sensitivity is strong, and it is gradually expanded to form the sliding surface [6]. Hence, the process of earthquakes action is the process of continuous damage of slope soil microstructure, continuous accumulation of residual deformation and continuous deterioration of soil mechanical properties [7,8].

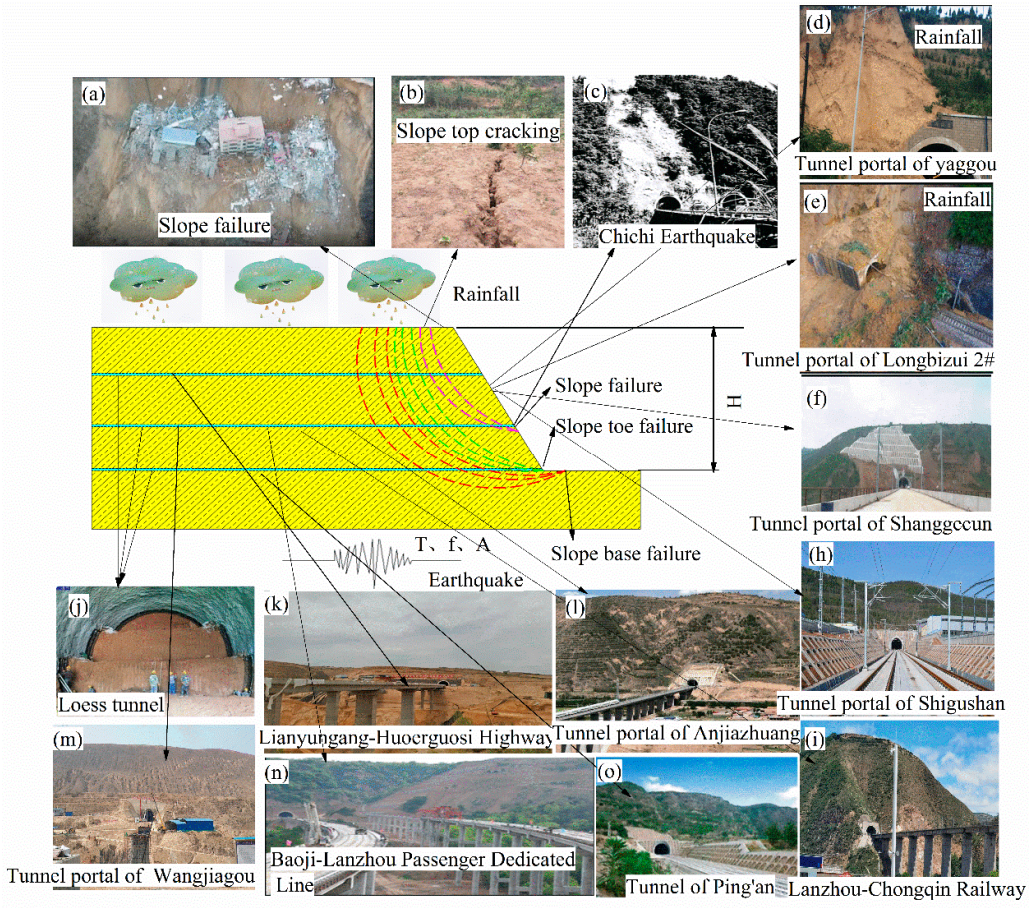

Figure 1. Loess portal mode, tunnel portal slope failure mode under earthquake and rainfall action. (**a**) Loess landslides; (**b**) Top of slope cracking; (**c**) Tunnel portal slope failure under earthquake action [21]; (**d**), (**e**) Tunnel portal slope failure under rainfall action; (**f**), (**h**) Tunnel portal slope; (**j**) Loess tunnel; (**i**), (**k**), (**l**), (**m**), (**n**), (**o**) Loess tunnels with different portal elevation.

According to statistics data showed that geological hazards occurred in loess areas account for one-third with China's [5]. In loess areas, earthquake-generated landslides and high-intensity earthquakes frequently occurred have led to enormous local casualties and economic losses. Under the seismic action, the PGA amplification effects at the bottom of the fracture development, free face, and the top in the loess slope were more significant than that in the others [3,7,9].

In recent years, a significant number of transportation tunnels, such as highway, high-speed railway, and subway tunnel engineering, have been and will be built successively in the Loess Plateau in China with high earthquake potential. Because of the complex topographical and geological conditions in Loess Plateau, the coverage of tunnels in the whole line is getting higher and higher, e.g., the tunnels in Zhengzhou-Xi'an high-speed railway covers only no more than 18% of the whole rail line with most of the tunnels in loess. However, the tunnels in Baoji-Lanzhou high-speed railway covers more than 68% of the whole line, and the tunnels and bridges covers more than 93% of the whole line. Therefore, many tunnels closely connecting high bridges passes through the upper slope surface instead of the slope foot (Figure 1k,l,n), the tunnels and bridges in Lanzhou-Chongqing Railway also covers more than 90% of the line in Gansu Province section(Figure 1i). The amplification effect was more significant with increasing of loess slope gradient and thickness [10]. Wu et al. [11,12] studied the failure mode and seismic response of the slope to a loess slope with and without fissure at the platform edge, and lower water content loess slope under earthquake actions via large-scale shaking table tests. Wang and Pu et al. [7,13] studied the deformation evolution and instability failure process of loess slope under the coupling of earthquake and rainfall. Cheng et al. [14] considered the unfavorable conditions of earthquake and rainfall, the seismic response rule of loess tunnel was studied using the shaking table tests. Sun et al. [15] the seismic responses and failure modes of the loess slope with bias tunnel were analyzed via shaking table tests. Liang et al. [16], Zhang et al. [17], Bian et al. [18], Fang et al. [19], and Wang and Liang et al. [20] studied the dynamic response characteristics of loess slope and the law of stress distribution of tunnel structures with the consideration of different tunnel portal elevations and slope gradients, and proposed a seismic fortification length for the tunnel portal elevation. However, the variation of dynamic response of the loess slope with tunnel, damage mechanism and gradual damage degradation, damage patterns, and displacement characteristics of the tunnel portal slope under dynamic action of loess slopes with tunnel were insufficiently studied.

The tunnel portal section is the transition from shallow-buried to deep-buried and with low stability due to the complex geological conditions and stress field & also the resulted deformation. In addition, the portal section was very vulnerable to the threat of slope deformation and failure problems such as landslides and collapses under the action of earthquakes. Therefore, it was very important to study the dynamic stability of tunnel portal slope. At tunnel portals, the main failure modes tends to be slope failures (Figure 1c,d,e). Database of seismic damage to underground structures analysis shows that damage to tunnels can be greatly reduced with increasing overburden. Deep tunnels are safer than shallow tunnels under earthquake action [22]. However, among the 57 tunnels investigations of mountain tunnels after the Chi-Chi Earthquake revealed that 16 tunnels suffered portal failure. When surface slopes fail during an earthquake, and tunnels portal can be damaged by the failure surface as well [23]. Tunnels with a small overburden at the portal are often undergo significant deformation under earthquake action compared with deep-buried tunnels. However, the soil pressure generated by ground deformation in a small overburden at the tunnel portal will be exerted on the tunnel lining structure as a horizontal force and will cause bending and tensile stress [22]. Analysis the dynamic stress and deformation of tunnel portal by numerical simulation indicate that the bending moment of the tunnel lining structure in the portal is much larger than that of the inner parts. [24]. Some damages about railway tunnels in the 2004 Niigata Earthquake shows that damages main occurred in the shallow tunnels and tunnel portal sections [25]. If a tunnel portal is located at the shallow-buried areas, the slope surface and tunnel lining structure will absorb much stronger seismic energy due to the refraction or reflection of seismic waves at ground surface [26]. The investigation of the seismic damage to the mountain highway tunnel in the Wenchuan earthquake demonstrated that had severe damaged to the tunnel portal section because of the

 doi:10.20944/preprints202309.1122.v1

landslide and rock-fall of the slope [27,28], and even the instability of the slope led to traffic interruption. Asakura et al. [29] classified the damage patterns of mountain tunnels by earthquake into three patterns, i.e. damaged in tunnel portals, damage of tunnels at a fractured zone, and damage of tunnels by sliding off a fault. The dynamic response characteristics of the tunnel entrance slope were related to the physical and mechanical properties of rock-soil mass and the propagation characteristics of the seismic waves in the rock-soil mass lower part of the tunnel [30]. Hence, the existence of a tunnel further complicated the dynamic response and stability of slope engineering.

In summary, the portal section of the tunnel is often shallow-buried, which is easy to be damaged and has a great influence on the whole line. The stress state of different parts of the slope is quite difference, and the stress and stability of the tunnel are different with the tunnel portal elevations. Under the earthquake action, there is a ground motion amplification effect on the slope, and the existence of the tunnel will affect this amplification effect. Meanwhile, the amplification effect of the slope will affect the dynamic response of the tunnel as well. There are more and more projects connected with high bridges and high tunnels portal in China, typical cases are shown in Figure 1f - 1n. The research of the tunnels in the upper slope connecting the high bridges are less compared with the tunnel portal at the slope toe. (Figure 1o).

The slope response owing to ground motion main involved in velocity, acceleration, displacement, dynamic stress, strain, and so on. Numerical simulations [7,24,31–35] and physical model tests [15,32,34–37] have been the primary methods to study the dynamic response of loess slopes. Shaking table tests are helpful for accurately and dynamically reflecting slope response under seismic loading. Analysis of the surface displacement had been a very visible, direct, and reliable method to reflect the dynamic deformation and failure of slopes. In particular, the displacement data acquisition is carried out by non-contact photographic technology, with no interference by seismic loading [38]. In the study, a loess slope with a high-speed railway tunnel across northwestern China is taken as the engineering background. Two different seismic wave and input directions, and 3D non-contact optical measurement techniques are applied to investigate the displacement of dynamic response characteristics of the tunnel portal sections loess slope. The damage mechanism, gradual damage degradation and crack development of the slope are discussed. The peak acceleration variation of the loess slope with a tunnel is analyzed on both the surface and inside the slope. The dynamic response law of the slope surface is interpreted to combine with numerical simulation.

2. Tests design

2.1. Project overview

This paper presents a typical case study on a 1352 m length of high-speed railway from chainage 30 + 745 to 32 + 097. The tunnel is a single-hole double-line, and the maximum buried depth is about 165 m. Figure 2a is the geological section. The ground elevation is between 1791 m and 2010 m. The stratum lithology of the tunnel site area is Malan loess of Quaternary Epipleistocene (Q_3), and Lishi loess of Quaternary Mediopleistocene (Q_2). The average annual precipitation is 292.0 mm, the maximum annual precipitation is 486.8 mm, and the minimum annual precipitation is 186.0 mm. The average annual evaporation is 1628.5mm. The maximum diameter of the prototype tunnel of D = 14.22 m (Figure 2b), slope elevation was about 9D, and slope gradient was about 60°. The tunnel is located at 1/3H of the slope.

Preprints (www.preprints.org) | NOT PEER-REVIEWED | Posted: 18 September 2023 doi:10.20944/preprints202309.1122.v1

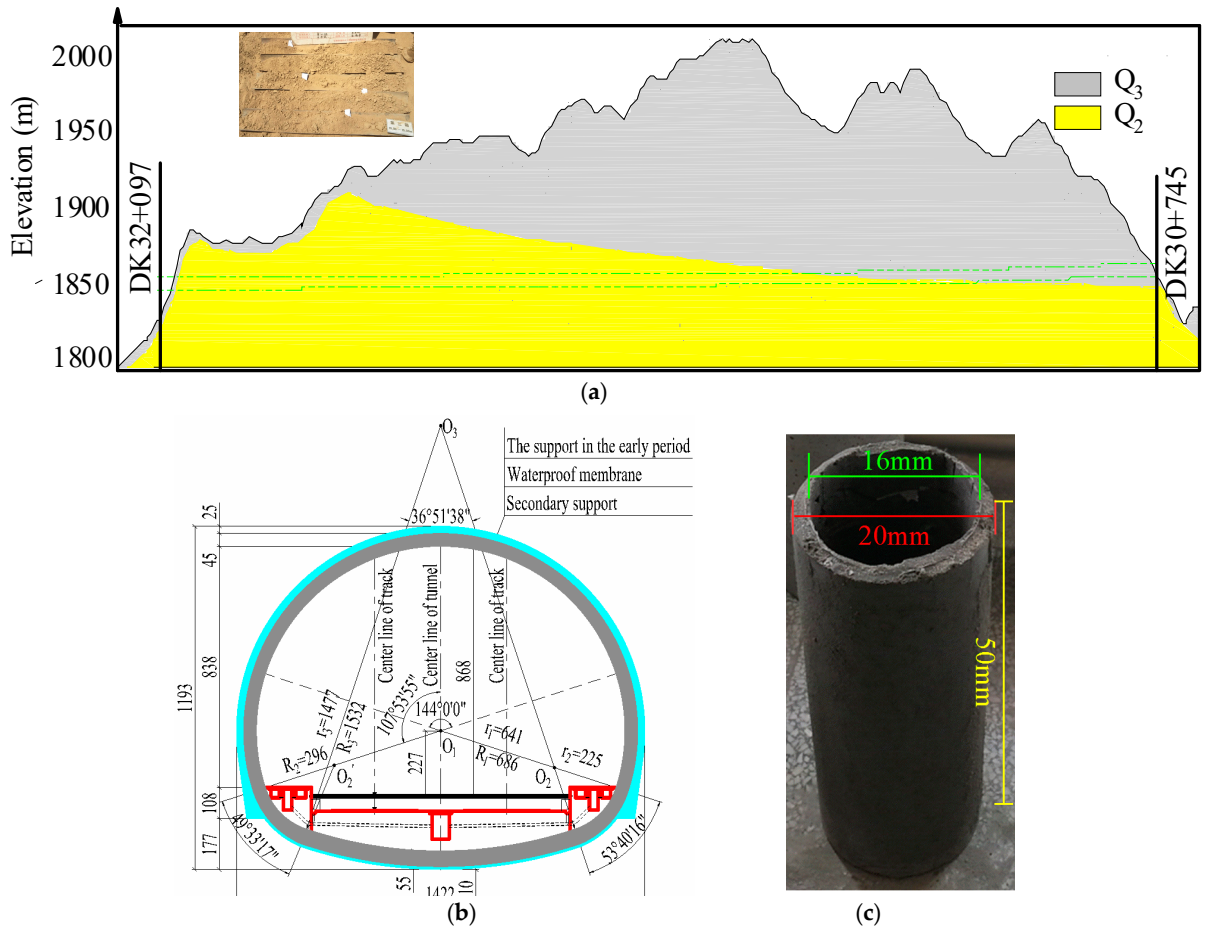

Figure 2. Tunnel cross-section and model. (**a**) Geological section; (**b**) Tunnel cross-section (unit: cm); (**c**) Tunnel model.

2.2. Model overview and design of similar material

The tunnel model is simplified as a circular lining with an inner diameter of 16 cm and length of 1 m (2 × 50 cm), which was made of 0.8 mm steel wire mesh and gravel concrete with an aggregate diameter of 2 - 5 mm and thickness of 2 cm. The tunnel model is shown in Figure 2c. The geometric similarity ratio and density similarity ratio is C_L = 80 and C_ρ = 1, respectively. The vibration acceleration similarity constant is C_α = 1 in the model test determined according to the similarity theory and model box size (length × width × height: 2.8 m × 1.4 m × 1.9 m; Figure 2c). The similarity coefficients of the other critical physical quantities are deduced according to the π theorem and dimensional analysis method, and the similarity relationship, as shown in Table 1. According to a series of laboratory tests, the simulated loess materials are main formed of loess, barite powder, sawdust (0.5 mm sieve), and water at the ratios of 0.835: 0.04: 0.015: 0.11. The physical properties of the test materials are listed in Table 2. The filling of the model soil is controlled thickness of 0.3 m in each layer. The water content and dry density of each layer are measured by ring knife sampling, and the dry density is controlled in the range of 1.5 g/cm^3. The slope gradient is 60°.

Preprints (www.preprints.org) | NOT PEER-REVIEWED | Posted: 18 September 2023 doi:10.20944/preprints202309.1122.v1

Table 1. Primary similar relationship of the model.

Physical quantity	Dimension	Similarity	prototype: model
Physical dimension: L	$[L]=[L]$	C_L	80
Density: ρ	$[\rho]=[M][L]^{-3}$	C_ρ	1
Acceleration of vibration: α	$[\alpha]=[L][T]^{-2}$	$C_\alpha=C_L{}^{-1}C_\rho{}^{-1}C_E$	1
Cohesion: c	$[c]=[M][L]^{-1}[T]^{-2}$	C_c	80
Internal friction angle: φ	/	C_φ	1
Poisson ratio: μ	$[\mu]=[1]$	C_μ	1
Modulus of elasticity: E	$[E]=[M][L]^{-1}[T]^{-2}$	C_E	80

Table 2. Material physical and mechanical parameters.

Sample type	ρ_d (g/cm³)	c (kPa)	φ (°)	ω (%)
Prototype soil	1.5	22.4	29.8	11
Actual model soil	1.5	23.5	28.9	11

The tests are performed in the Key Laboratory of Loess Earthquake Engineering, Gansu Earthquake Administration. An electric servo shaking table using in the tests is 6 m long and 4 m wide (6 m × 4 m), with 12 horizontal and 16 vertical motors to apply the bi-directional (horizontal and vertical) loading, as shown in Figure 3a. The maximum horizontal and vertical accelerations are 1.7g and 1.2g, respectively. The maximum horizontal and vertical speeds are 1.5 m/s and 0.7 m/s, respectively. The frame was made of section steel on both sides of the model box, and transparent organic glass is used as a baffle to observe crack development during the tests. The bottom of the box and rear baffle are steel plates. The treatment of the model box boundary is as follow: the rear baffle adopt a polyethylene foam board as a buffer material to reduce the influence of the boundary on the input seismic wave, and pebble-bonded cement mortar is added at the bottom to simulate the bedrock, as shown in Figure 3c.

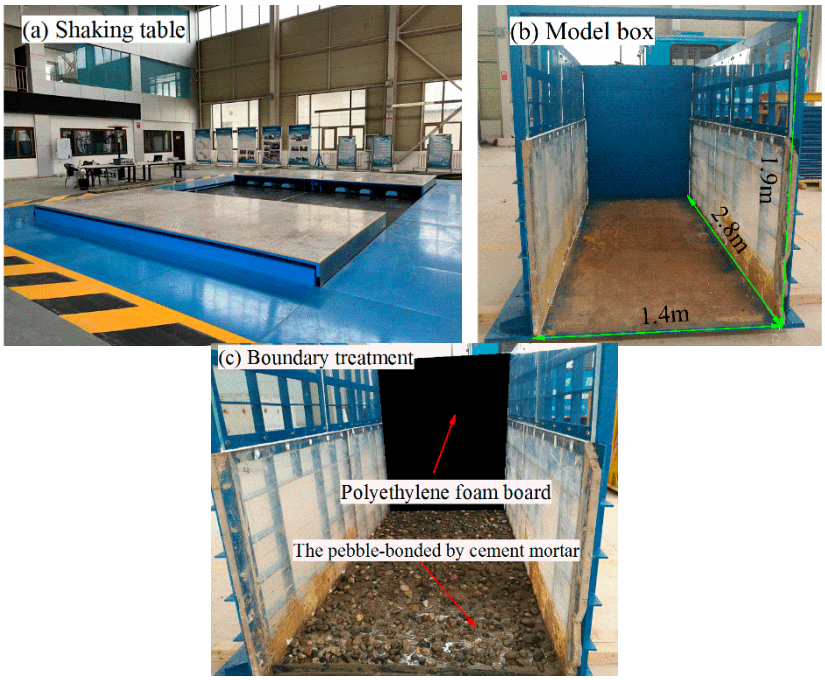

Figure 3. Shaking table and model box. (**a**) Shaking table; (**b**) Model box; (**c**) Boundary treatment of model box.

Preprints (www.preprints.org) | NOT PEER-REVIEWED | Posted: 18 September 2023 doi:10.20944/preprints202309.1122.v1

2.3. Arrangement of acceleration sensors

In order to study the dynamic response of the slope with the tunnel at the surface and interior, 26 Donghua DH301 capacitive acceleration sensors were installed in the model, including 8 on the slope surface, 2 on the top of slope, and 10 around the tunnel. The rest were installed in the interior of the slope. The acceleration sensors were embedded into the middle of the longitudinal section of the model in order to reduce the influence of the side boundary effect. The completed model and layout of the acceleration sensors were shown in Figure 4a,b.

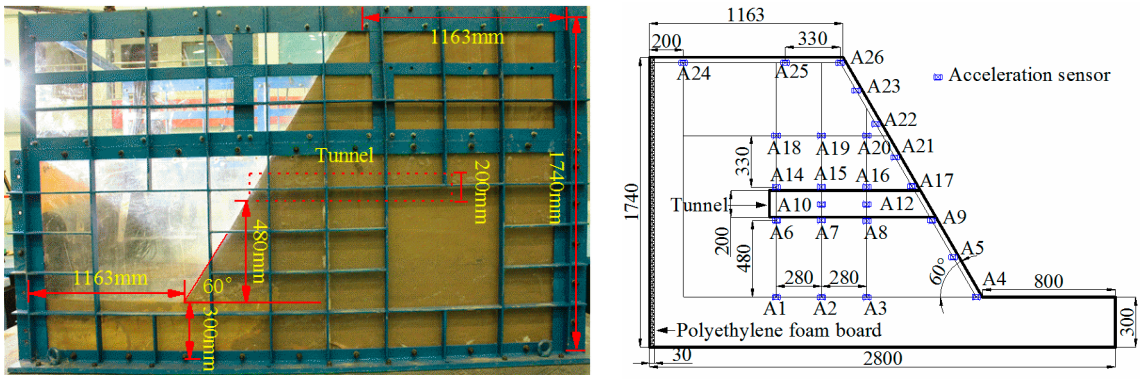

(**a**) (**b**)

Figure 4. Completed box and layout of acceleration sensors. (**a**) Completed box; (**b**) Layout of acceleration sensors (unit: mm).

2.4. Optical displacement measurement system

To track the displacement of the slope surface subjected to seismic loading, the displacement data were collected by using the XTDIC measurement system based on binocular stereo vision technology. The XTDIC measurement system and layout of it was shown in Figure 5a,b. The system consisted of two cameras with a resolution of two million pixels, lighting equipment, and an acquisition computer. One camera was used to collect the displacement data of the slope surface in the Y and Z directions, and the other camera was used to collect the displacement data of the slope surface in the X and Z directions. It had an acquisition frequency of 50 Hz, and the accuracy was 0.05 mm. The patch marking points were radially arranged on the slope with the tunnel as the center, and the radial spacing was approximately 100 mm. The three-dimensional (3D) displacement of every marked point was obtained in the tests, and the layout of the measurement points were shown in Figure 6a,b.

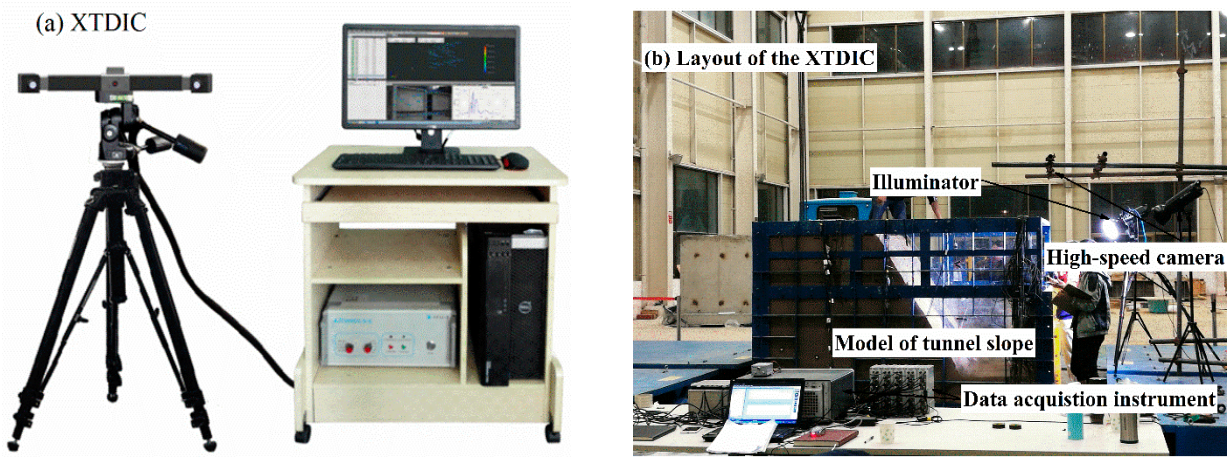

Figure 5. XTDIC measurement system. (**a**) XTDIC optical measurement system; (**b**) Layout of XTDIC measurement system.

Preprints (www.preprints.org) | NOT PEER-REVIEWED | Posted: 18 September 2023 doi:10.20944/preprints202309.1122.v1

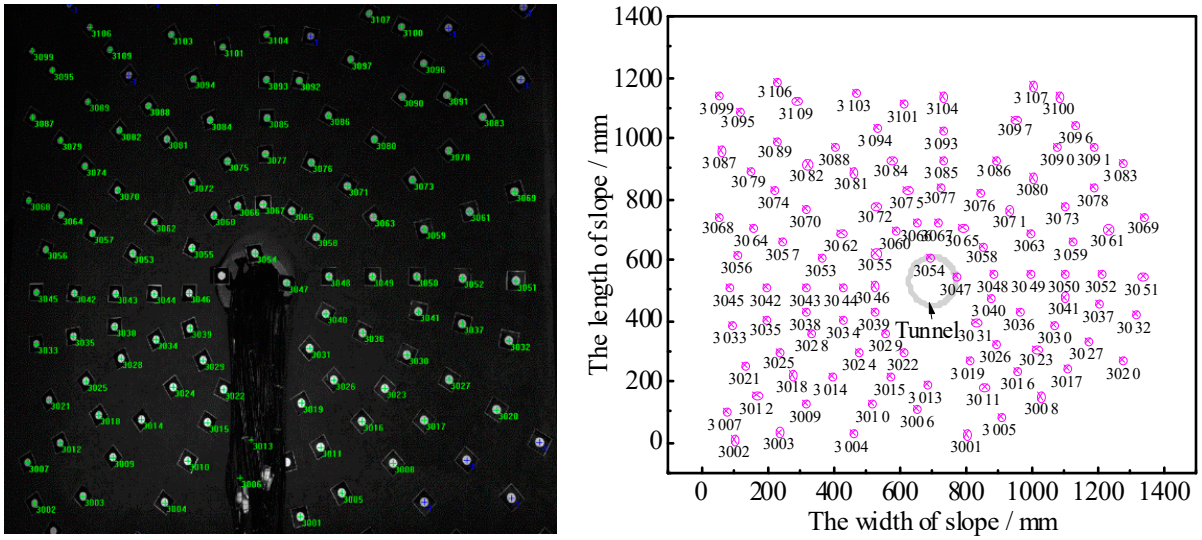

(a) (b)

Figure 6. Layout of measurement points of surface displacement. (**a**) Measurement points; (**b**) Sketch map.

2.5. Seismic waves and loading conditions

The input seismic waveforms in the tests were Wenchuan-Tangyu wave (WT wave) and El Centro wave (El wave), and the input direction was divided into the horizontal (X), the combined action of horizontal and vertical (X-Z) seismic loads, where X was the direction along the tunnel, and Z was the vertical or gravitational direction. The variation and dynamic response characteristics of the slope surface displacement were obtained under different seismic waveforms and direction. The amplitude was increased from 0.1g to over 0.4g, and the corresponding seismic intensity was increased from VII to over IX. The specific loading sequence was shown in Table 3. The seismic wave was simulated by inputting an acceleration time-history curve in the process of shaking table tests. The acceleration time history curves of the two seismic waveforms were shown in Figure 7a,b. The model failed upon loading to SN13 (WT 698 gal (X)).

Table 3. Loading conditions of the tests.

Conditions / SN	Corresponding basic intensity	Amplitude / g	Seismic waveforms	Peak ground acceleration in loading direction / gal
SN1	VII (0.09~0.17g)	0.1	WT wave	116 (X)
SN2			WT wave	116 (X), 78 (Z)
SN3			El wave	117 (X)
SN4			El wave	117 (X), 54 (Z)
SN5	VIII (0.18~0.35g)	0.2	WT wave	233 (X)
SN6			WT wave	233 (X), 156 (Z)
SN7			El wave	235 (X)
SN8			El wave	235 (X), 107 (Z)
SN9	IX (0.36~0.40g)	0.4	WT wave	465 (X)
SN10			WT wave	465 (X), 312 (Z)
SN11			El wave	470 (X)
SN12			El wave	470 (X), 215 (Z)
SN13	Over IX (0.41~0.70g)	Over 0.4	WT wave	698 (X)

Preprints (www.preprints.org) | NOT PEER-REVIEWED | Posted: 18 September 2023 doi:10.20944/preprints202309.1122.v1

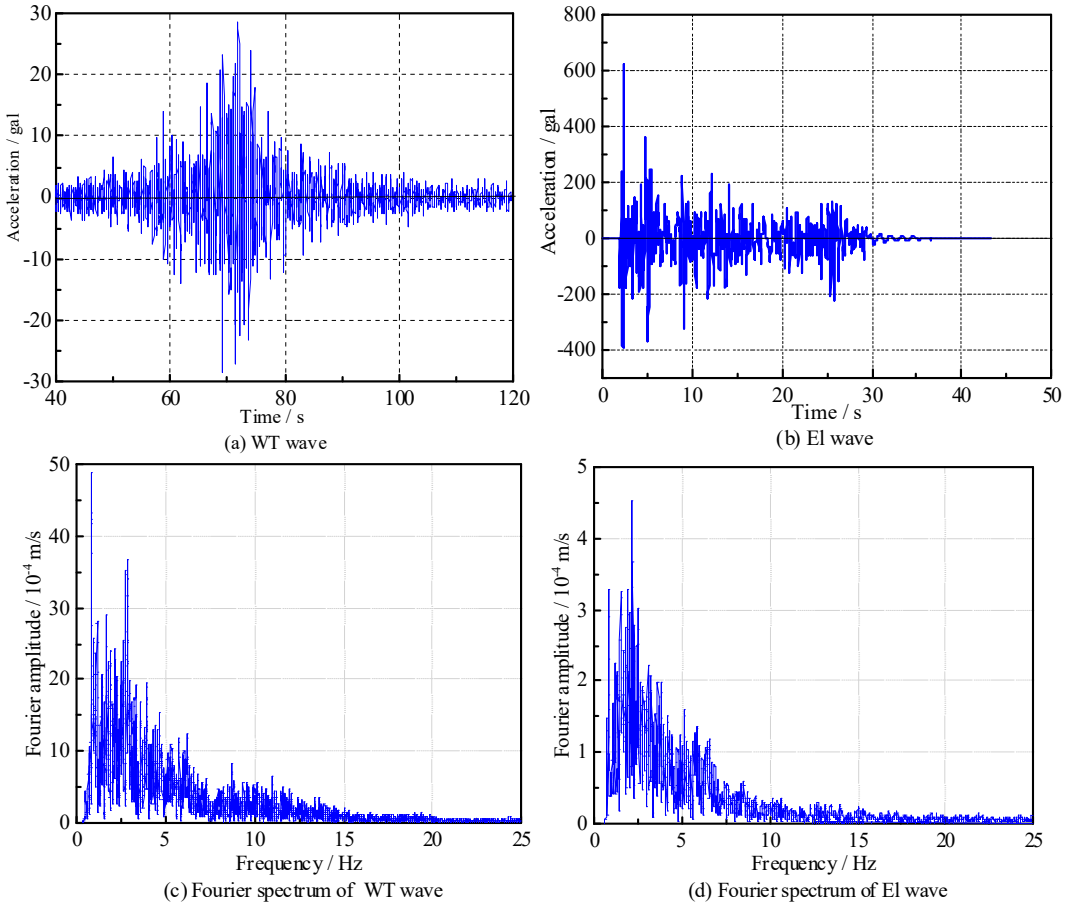

Figure 7. Acceleration time history curve and Fourier spectrum of the seismic wave. (**a**) Acceleration time history curve of WT wave; (**b**) Acceleration time history curve of El wave; (**c**) Fourier spectrum of WT wave; (**d**) Fourier spectrum of El wave.

3. The PGD distribution of the slope surface and dynamic damage development of the slope

For an earthquake-induced slope failure, the displacement was one of the important factors for definition of failure [39]. The displacement generated by the marking points within the range of 1400 mm wide and 1200 mm height (1400 mm ×1200 mm) was chosen, and the slope surface displacement nephogram was drawn. The horizontal and vertical axes represented the slope width within the selected range and the direction from the bottom to the top of the slope, respectively. The color gradation represented the displacement magnitude of the slope surface. The peak ground displacement (PGD) was the peak value of displacement at each measuring point. The displacement data in the slope surface displacement nephogram was the PGD under the corresponding loading conditions. In the tests, the slope surface was mainly displaced in the X and Z directions when the input seismic wave was created in X direction, X and Z biaxial directions (X-Z directions). Therefore, the input seismic wave in X direction and X-Z directions collected the settlement deformation (PGD_Z) and the sliding deformation (PGD_X), respectively. The PGD was not obtained at SN13, because some marking points of the slope surface had fallen off.

The peak value of the slope surface with the input in different directions and different waveforms were shown in Table 4. For the comparative analysis, the same peak acceleration was set in the horizontal direction when input wave was X direction and X-Z direction. The peak acceleration in X direction input seismic wave was 2.18 times and 1.49 times in Z direction for El wave and WT wave when input wave was X-Z direction, respectively. In addition, the PGD_X measured was much larger than that of the PGD_Z when the input wave was in the X direction. The input peak acceleration in the X direction was larger than that of the Z direction when the input wave was in the X-Z direction. However, the PGD_X and the PGD_Z measurement of it presented a good similarity with which the input wave was in the X direction. Overall, the PGDX and PGD_Z of the slope surface increased with

Preprints (www.preprints.org) | NOT PEER-REVIEWED | Posted: 18 September 2023 doi:10.20944/preprints202309.1122.v1

the increasing of the input peak ground acceleration when the input wave was same waveform and same direction. On average, the PGDx was approximately 2.69 - 5.11 times and 2.79 - 2.97 times as large as the PGDz when the input WT wave and El wave was in the X direction, respectively. Whereas, the average PGDx was approximately 1.63 – 1.97 times and 2.52 - 2.63 times as large as the average PGDz when the input WT wave and El wave was in the X-Z direction, respectively. Therefore, the horizontal deformation was the primary deformation, and the X direction seismic wave had a greater impact on the deformation of the slope. Taking the WT wave as an example, The PGD distribution of the slope surface with the input in different directions were shown in Figure 8a–f and Figure 9a–c. It showed that the PGD increased with the increasing of the peak ground acceleration in the same waveform and same direction. When the peak ground acceleration was 0.1 g, the PGD was small, and the slope was stable. However, when the peak ground acceleration was 0.4, the PGD increased rapid, indicating that a large deformation appeared in the slope surface.

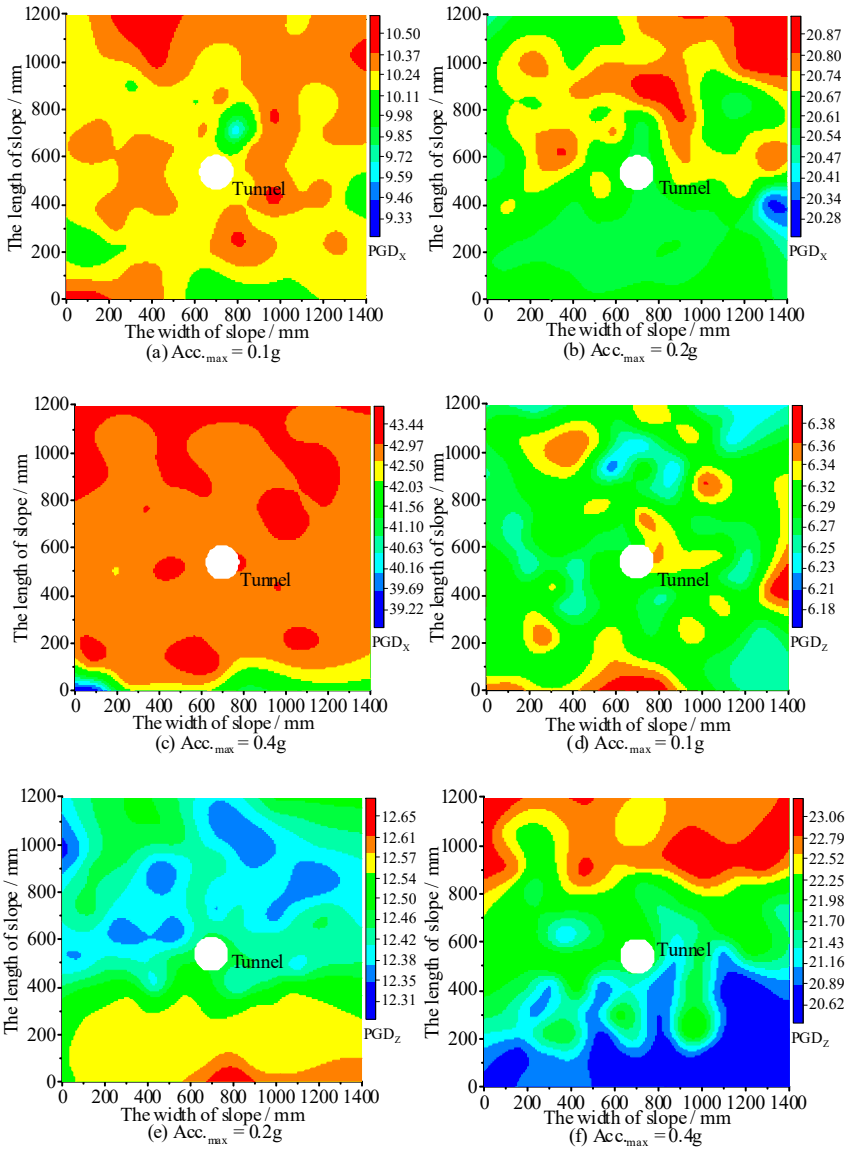

Figure 8. PGD distribution of the slope surface when the input WT wave was in X-Z direction. (**a**) Acc.max=0.1g, PGDx; (**b**) Acc.max=0.2g, PGDx; (**c**) Acc.max=0.4g, PGDx; (**d**) Acc.max=0.1g, PGDz; (**e**) Acc.max=0.2g, PGDz; (**f**) Acc.max=0.4g, PGDz.

Preprints (www.preprints.org) | NOT PEER-REVIEWED | Posted: 18 September 2023 doi:10.20944/preprints202309.1122.v1

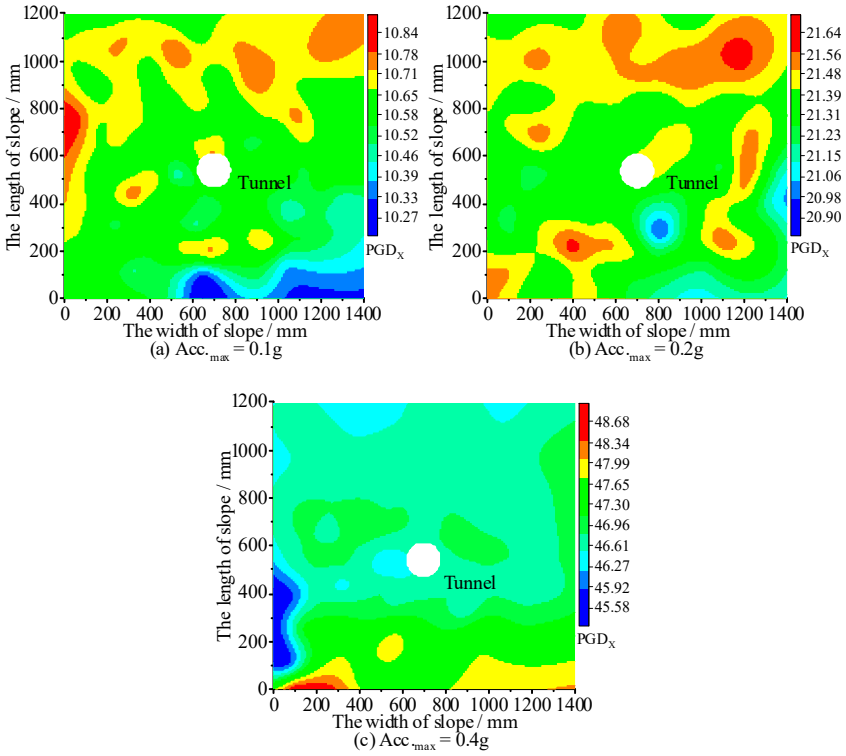

Figure 9. PGD distribution of the slope surface when the input WT wave was in X direction. (**a**) Acc.max=0.1g, PGDx; (**b**) Acc.max=0.2g, PGDx; (**c**) Acc.max=0.4g, PGDx.

Table 4. Slope surface and cracks behavior under each loading condition.

Conditions	SN	$PGD_{X\text{-}max}$ (mm)	$PGD_{X\text{-}min}$ (mm)	$PGD_{Z\text{-}max}$ (mm)	$PGD_{Z\text{-}min}$ (mm)	The law of slope surface
0.1g	SN1	10.54	10.27	4.04	3.66	PGD of the slope surface difference was small.
	SN2	10.50	9.33	6.38	6.18	
	SN3	6.94	6.40	2.43	2.31	
	SN4	7.25	6.65	2.80	2.67	
0.2g	SN5	21.64	20.90	7.81	7.18	PGD of the slope surface difference was small.
	SN6	20.87	20.28	12.65	12.31	
	SN7	14.03	13.16	4.87	4.71	
	SN8	14.36	13.79	5.42	5.25	
0.4g	SN9	48.68	45.58	11.14	8.45	Chip off-falling at the foot of the slope.
	SN10	43.44	39.22	23.06	20.62	Approximate horizontal cracks appeared in the middle and upper slope above the tunnel, the foot of the slope was loose, and soil mass fell.
	SN11	32.84	26.62	9.81	9.58	Cracking and peeling appear on the slope surface.
	SN12	35.06	28.40	12.06	9.11	A large area of chip off-falling appeared on the slope, PGD of the slope surface also showed an elevation amplification effect.
Over 0.4 g	SN13	/	/	/	/	The slope collapsed.

Note: $PGD_{Z\text{-}max}$ - The maximum value of PGDz; $PGD_{Z\text{-}max}$ - The minimum value of PGDz; $PGD_{X\text{-}max}$ - The maximum value of PGDx; $PGD_{X\text{-}max}$ - The minimum value of PGDx.

Preprints (www.preprints.org) | NOT PEER-REVIEWED | Posted: 18 September 2023 doi:10.20944/preprints202309.1122.v1

The dynamic damage process of the tunnel entrance slope was shown in Figure 10a–e. Due to the dynamic load could loosen loess soil mass, which reduced the shear strength of loess soil mass, plastic deformation gradual increased, leading to cracking of loess slope, and residual displacement (RD) accumulated was larger in Z direction than that of in X direction. The tension cracks first occurred on the left of the slope top near the rear baffle of the model box and was developing from left to right. The top of slope cracks exhibits main tension and shear processes. Slope surface of the deformation difference between PGD_{max} and PGD_{min} increased with the increasing of the peak ground acceleration in the same seismic wave and direction, indicating that the deformation of the surface slope increased as well. The failure of tunnel entrance slope was mainly induced by the horizontal wave. As shown in Figure 10b–e, a larger horizontal shear deformation of the loess slope induced by the strong horizontal shaking from the X direction wave, which led to shear cracks and the sliding deformation of the surface slope. Compared with the X-direction wave, the X-Z direction wave increased the vertical vibration of the slope and the lateral cracks was induced on the slope surface, and the difference settlement deformation was also observed, which weakened loess slope stability above the tunnel (Figure 10d). Slope surface cracks main concentrated on the middle and upper sections of it. Meanwhile, it could be seen from Figure 10a–e, the slope surface and top of the slope many penetrating cracks also appeared, and top of the slope produced a large deformation and began to fail due to large settlement difference, and the tunnel entrance slope was destroyed under the action of a large horizontal seismic acceleration finally. The reason was that the multi-times dynamic disturbance on the soil, resulting the loss of cementation between the particles in the loess and the disintegration of the aggregates, the damage of the loess structure and the decrease of the strength, the crack was first formed at the position where the disturbance sensitivity was strong, and it was gradually expanded to form the sliding surface. Even if there is no stronger seismic action, the loess slope is more likely to cause instability and failure encountering rainfall after cracking. Some feature points of center of the slope surface were selected to analyze the change of PGD under each loading condition, as shown in Figure10f. The PGD value of each point and the change rule on the slope surface was consistent both the X direction and Z direction, respectively. The tension crack, the shear sliding surface running through the entire slope, and the mutation of displacement and acceleration response may be regarded as the criterion of estimating slope dynamic failure [40]. The PGD_X suddenly increased under SN9 loading condition. Meanwhile, the PGD_X mutation was consistent with cracking of the slope under this condition. It indicated that the loess slope with tunnel had been dynamic failure.

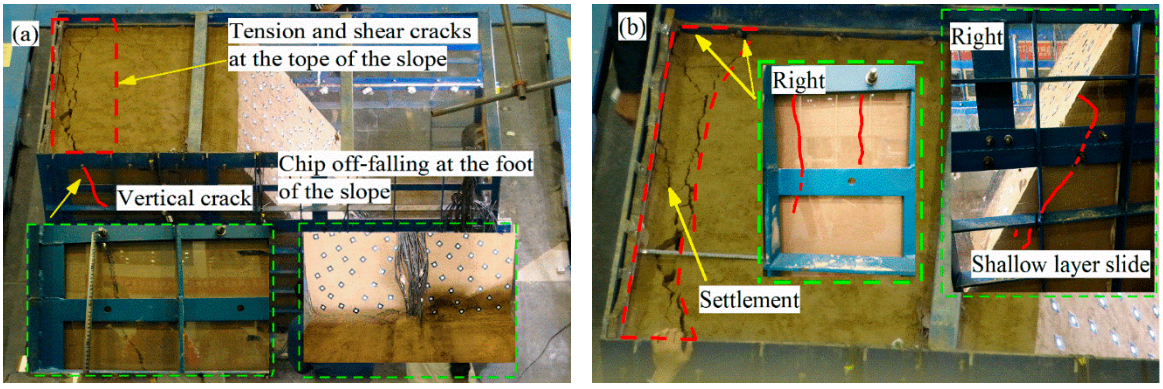

Preprints (www.preprints.org) | NOT PEER-REVIEWED | Posted: 18 September 2023 doi:10.20944/preprints202309.1122.v1

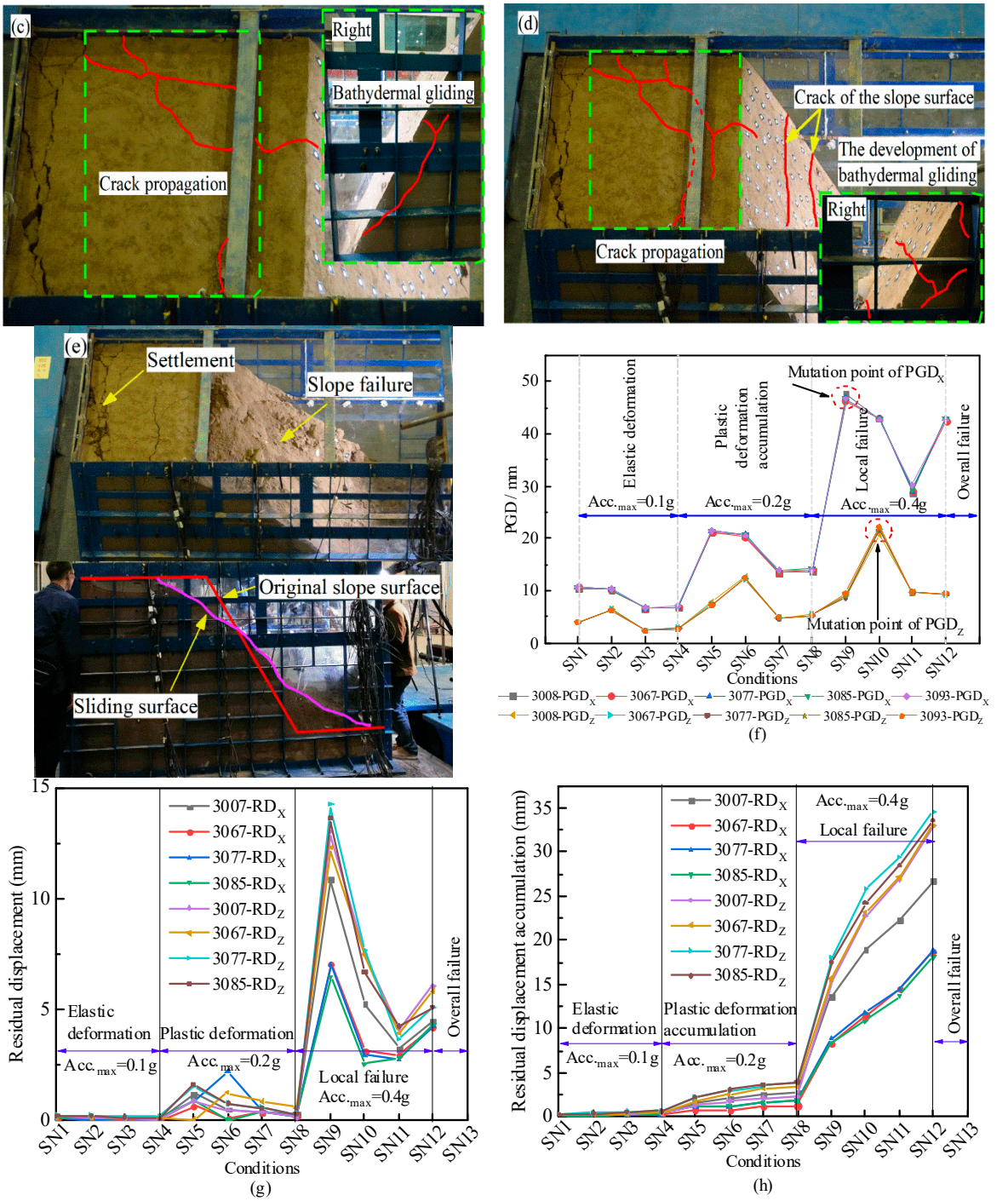

Figure 10. Dynamic damage development of the tunnel entrance slope. (**a**) SN9 (WT wave 465 gal (X)); (**b**) SN10 (WT wave 465 gal (X), 312gal (Z)); (**c**) SN11 (El wave 470 gal (X)); (**d**) SN12 (El wave 470 gal (X), 215 gal (Z)); (**e**) SN13 (WT wave 698 gal (X)); (**f**) The change of PGD under each loading conditions; (**g**) The change of residual displacement under each loading conditions; (**h**) The change of residual displacement accumulated under each loading conditions.

Because the duration of the WT wave was longer than that of the El wave, the PGD of the slope surface was more significant for the input WT wave than that of the El wave. Combined with the development of displacement and cracks on the slope surface for tunnel entrance slope, the test results showed that the deformation and failure processes of the tunnel entrance slope could be divided into four stages:

Preprints (www.preprints.org) | NOT PEER-REVIEWED | Posted: 18 September 2023 doi:10.20944/preprints202309.1122.v1

(1) When the amplitude of the peak ground acceleration was 0.1g, the average PGD of the slope surface was small, no cracks could be found on the slope surface, and residual displacement was very small. This was the stage of elastic deformation. As shown in Figure 10f,g,h.

(2) When the amplitude of the peak ground acceleration was 0.2g, the slope surface displacement gradually increased with the increasing of seismic loading. Although no visible cracks appeared on the slope surface, the residual deformation gradual accumulated. This was the stage of plastic deformation accumulation. As shown in Figure 10h.

(3) Cracks first appeared at the top of the slope for the loess slope with tunnel under loading condition of SN9. Meanwhile, PGDx of mutation the slope surface indicated the slope failure, and critical horizontal displacement was 48 mm. When the amplitude of the peak ground acceleration was 0.4g, with the emergence & expansion of cracks and the shear failure of slope surface above the tunnel. The residual displacement (RD) accumulated was larger in Z direction than that of in X direction, it indicated that the slope began to downslide. This was the stage of local failure. As shown in Figure 8c,f, Figure 9c, Figure 10f,g,h.

(4) When the amplitude of the peak ground acceleration was over 0.4g, the displacement marking points of slope surface fell off, and the slope failed. This was the stage of overall failure. As shown in Figure 10e.

4. Analysis of acceleration response

4.1. Acceleration of the slope

The PGA distribution and peak value of the PGA was shown in Figures 11 and 12 and Table 5. The existence of the tunnel had a great influence to the PGA of the soil mass surrounding it. The PGA of the tunnel entrance slope increased with the increasing of the PGA of the input seismic wave. The input PGA in the X direction was approximately 1.49 times and 2.18 times as large as the input PGA in the Z direction when the input of WT wave and El wave was in the X-Z direction, respectively. On average, the PGA of the X direction (PGA_x) of the tunnel slope was approximately 1.21 – 1.45 times and 1.84 -2.14 times as large as the PGA of the Z direction (PGA_z) of the tunnel slope, respectively. Because the slope self-weight had an adverse effect to the amplification of the vertical acceleration. Taking the WT wave as an example, Figure 11a–c and Figure 12a–f showed that the PGA_x of the tunnel entrance slope when the input wave in the X-Z direction was larger than that the input WT wave in the X direction. In addition, the PGA of input wave was in X direction was larger than that the PGA of input wave was in Z direction, and the existence of the tunnel, which led to a restrained acceleration amplification effect of the PGA_z. Overall, from the PGA distribution of slope with tunnel, it could be seen that under the action of different seismic waves, and the obvious amplification effect appeared at the top of the slope and near the free surface.

Table 5. Peak value of the PGA.

Waveform	Direction	$Acc._{max}$	Peak value of the PGA			
			$PGA_{x\text{-}max}$	$PGA_{x\text{-}min}$	$PGA_{z\text{-}max}$	$PGA_{z\text{-}min}$
El wave	Put into X	0.1g	2.622	1.267	0.9785	0.009
		0.2g	4.724	2.074	1.669	0.008
		0.4g	10.073	3.877	4.168	0.010
	Put into X-Z	0.1g	2.409	1.326	1.378	0.009
		0.2g	4.804	2.493	2.809	0.011
		0.4g	11.342	4.308	6.036	0.007
WT wave	Put into X	0.1g	2.332	1.246	0.958	0.007
		0.2g	4.134	2.078	1.682	0.011
		0.4g	8.404	3.272	3.469	0.009
	Put into X-Z	0.1g	2.703	1.473	1.685	0.011
		0.2g	4.335	2.380	2.448	0.009
		0.4g	8.867	4.597	7.102	0.009

Note: $PGA_{z\text{-}max}$ - The maximum value of PGA_z; $PGA_{z\text{-}max}$ - The minimum value of PGA_z; $PGA_{x\text{-}max}$ - The maximum value of PGA_x; $PGA_{x\text{-}max}$ - The minimum value of PGA_x.

Preprints (www.preprints.org) | NOT PEER-REVIEWED | Posted: 18 September 2023 doi:10.20944/preprints202309.1122.v1

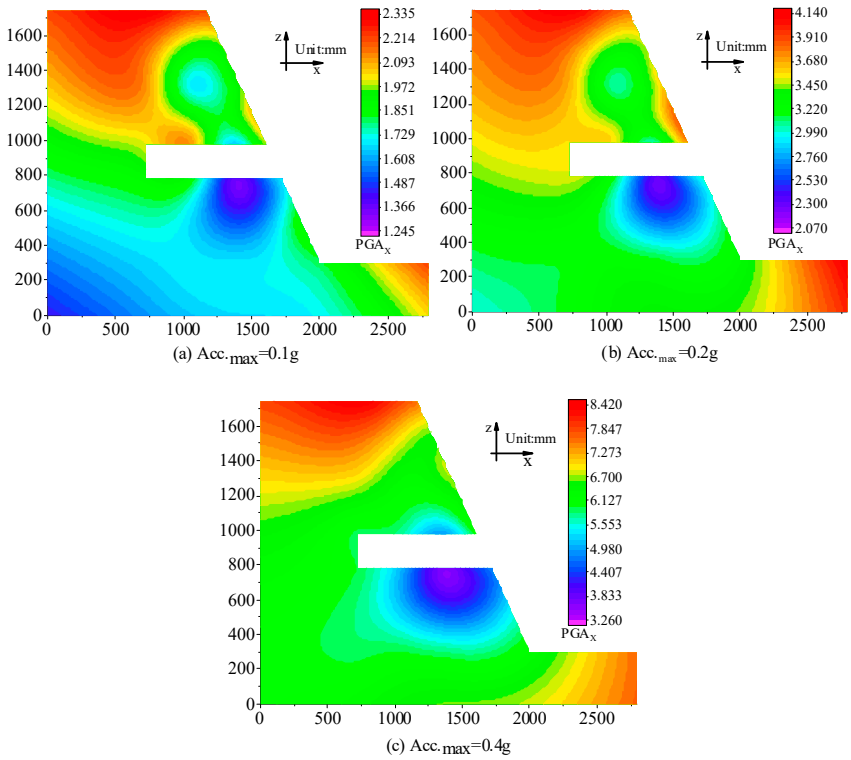

Figure 11. Distribution of the PGA when the input WT wave was in X direction. (**a**) Acc.$_{max}$=0.1g, PGAx; (**b**) Acc.$_{max}$=0.2g, PGAx; (**c**) Acc.$_{max}$=0.4g, PGAx.

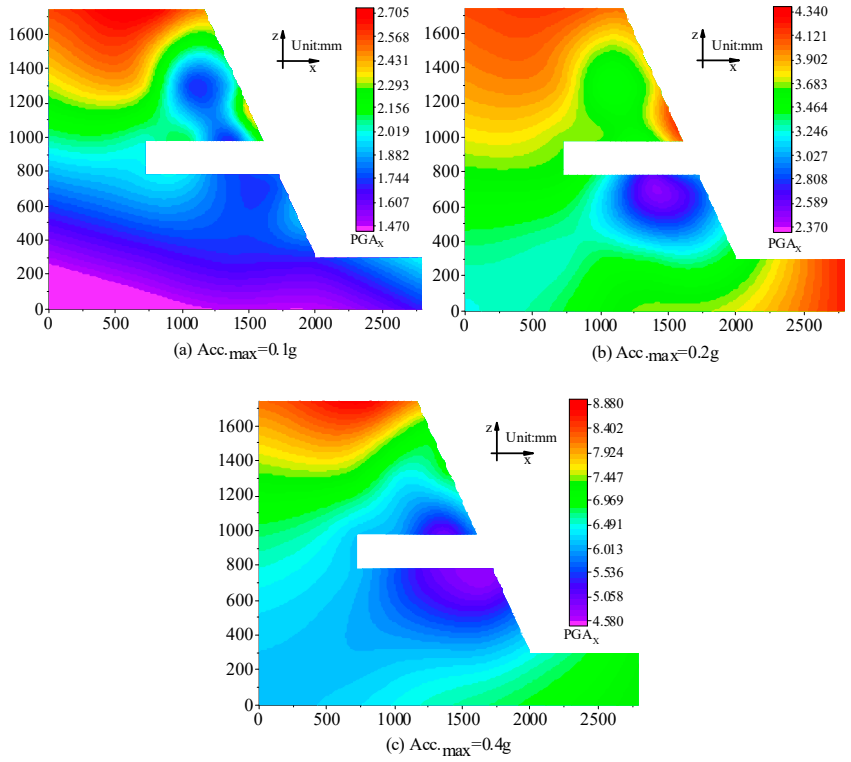

Preprints (www.preprints.org) | NOT PEER-REVIEWED | Posted: 18 September 2023 doi:10.20944/preprints202309.1122.v1

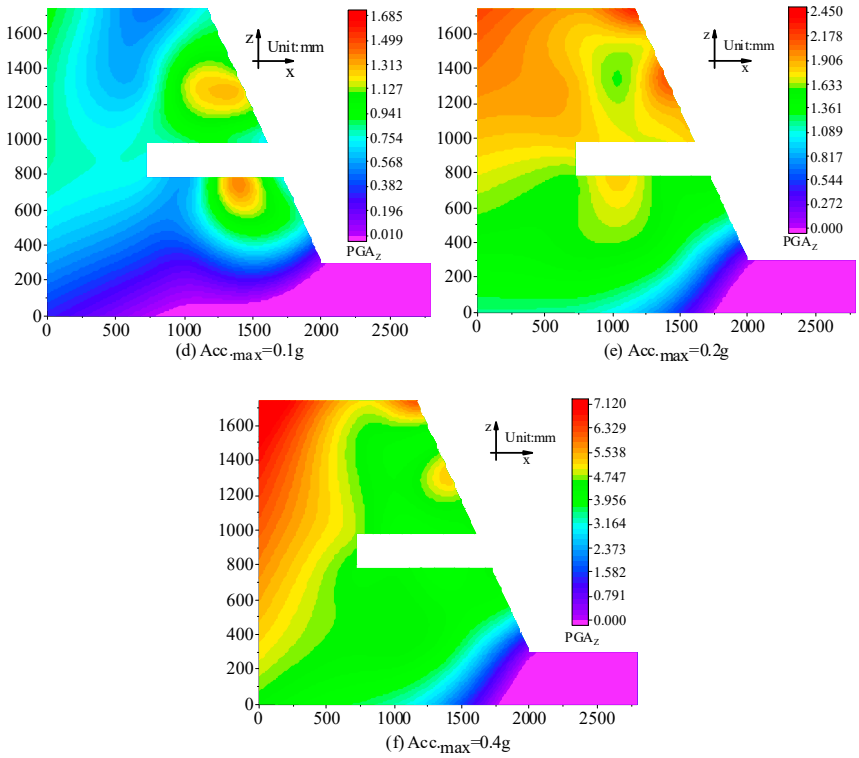

Figure 12. Distribution of the PGA when the input WT wave was in X-Z direction. (**a**) Acc.max=0.1g, PGAx; (**b**) Acc.max=0.2g, PGAx; (**c**) Acc.max=0.4g, PGAx; (**d**) Acc.max=0.1g, PGAz; (**e**) Acc.max=0.2g, PGAz; (**f**) Acc.max=0.4g, PGAz.

4.2. The PGA amplification factor of the slope

The ratio of the PGA at each measurement point to the peak acceleration on the shaking table was defined as the PGA amplification factor (PGAAF) to describe the slope acceleration response characteristic under seismic wave. The distribution of PGAAF was shown in Figure 13, and Figure 14a,b, when the input El wave and WT wave were in X and X-Z direction. The PGAAF of the tunnel slope increased non-linearly with the increasing of the PGA of the input seismic wave. The tunnel had a significant inhibitory to elevation amplification effect of the PGAAF distribution of the surrounding soil mass. This was because the seismic waves encountered the tunnel surface with clear differences in the physical properties of the medium during their propagation in the slope, thereby forming a strong reflection and refraction effect, and the amplitude changed significant. The seismic waves were scattered and refracted near the tunnel, resulting in the complex superposition of waves and amplitude decreased. The PGAAF of the slope in X direction was < 1 when the input peak acceleration of wave was 0.1 g, and the rest were more than 1. The PGAAF of the tunnel slope when the input wave in the X direction was larger than that in the X-Z direction. It could be seen that under the action of different seismic waves, the distribution of the PGAAF of the two types of input waveforms was basically the same, and the obvious amplification effect appeared at the top of the slope and near the empty surface. The PGAAF of the tunnel slope when the input wave was in the X-Z direction was larger than that in the X direction, indicating that the PGAAF amplification effect input wave in the X-Z direction was larger than that in the X direction.

Preprints (www.preprints.org) | NOT PEER-REVIEWED | Posted: 18 September 2023 doi:10.20944/preprints202309.1122.v1

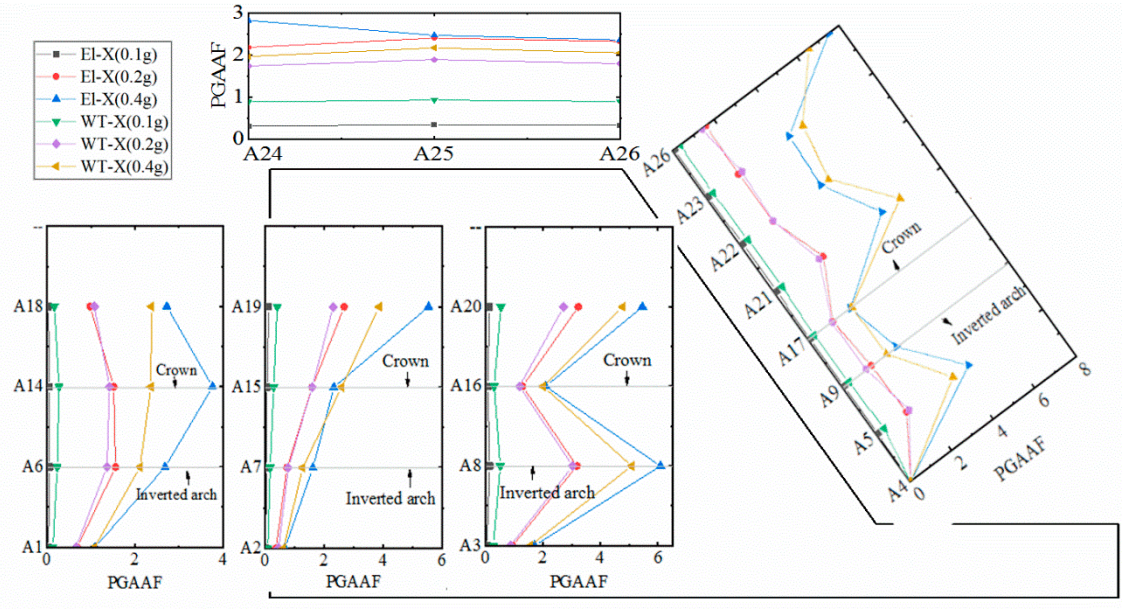

Figure 13. Input in X direction.

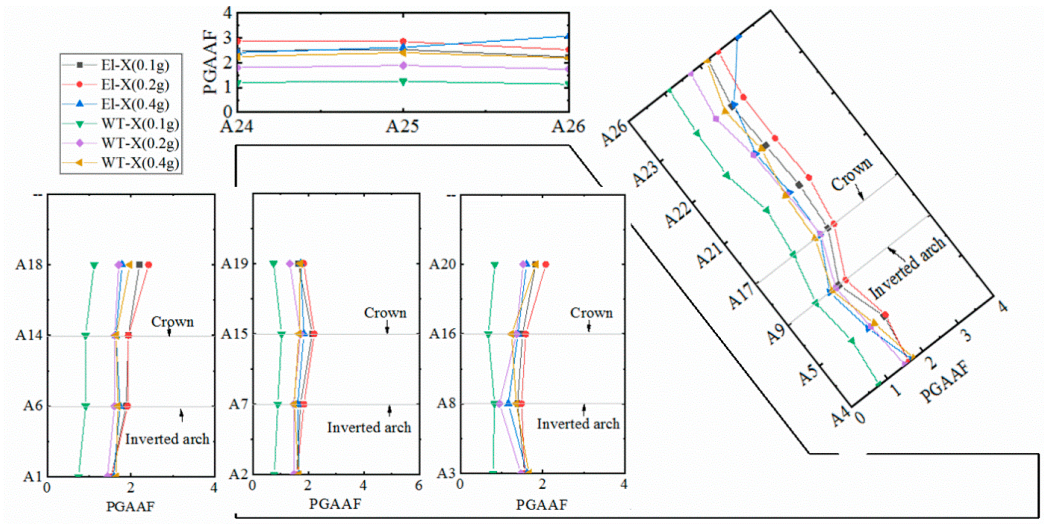

(**a**)

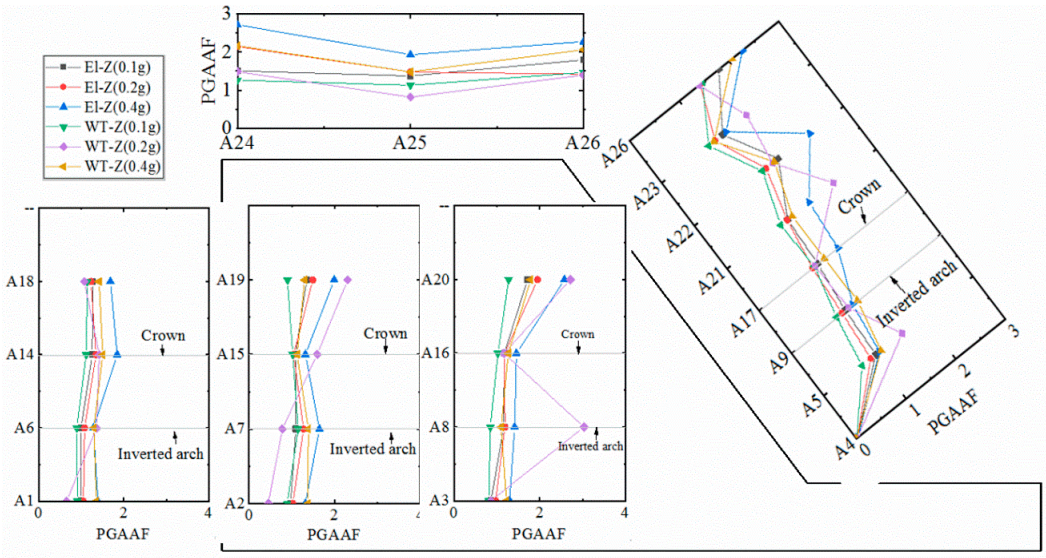

(**b**)

Figure 14. Input in X-Z direction. (**a**) PGAAF of the X direction; (**b**) PGAAF of the Z direction.

Preprints (www.preprints.org) | NOT PEER-REVIEWED | Posted: 18 September 2023 doi:10.20944/preprints202309.1122.v1

Overall, from the distribution of PGA with the tunnel-slope system, it could be seen that under the action of different seismic waves, the distribution of the PGA and the PGAAF was basically the same, the distribution of the PGAAF of the two types of input waveforms was basically the same as well, and the obvious amplification effect appeared both at the top of the slope and near the empty surface. The existence of the tunnel had a great influence to the PGA and the PGAAF of the soil mass surrounding it. Especially, the inhibition effect was the most obvious to the soil mass below the tunnel. However, this inhibition effect gradual weakened with the increasing of the seismic wave peak acceleration. Additionally, the failure of the slope with tunnel during the earthquake could be identified according to either the PGA, PGAAF, or PGD. Particularly, it could be obvious explained by using the PGD when the large deformation of the slope first occurred.

5. Numerical simulation of the dynamic response of the front slope of loess tunnel

5.1. Models and parameters

Using the finite element software MIDAS GTS/NX, the three-dimensional numerical simulation of the dynamic response of the front slope of the loess tunnel was carried out. There were the two slope models which were set up with the tunnel and without the tunnel, respectively. The slope gradient, model size, physical and mechanical parameters of the two slope models were the same. The slope gradient were 60°. The model size was 100m in the Y direction, 224 m in the X direction, and 139 m in the Z direction (height of slope was 115 m), respectively. The portal elevations was set at 1/3 height of the slope (38.3 m) for the slope model with the tunnel, and the maximum portal diameter was 14.22 m. The physical and mechanical parameters were shown in Table 6. The elastic modulus of primary lining was obtained by reduction calculation of the shotcrete and steel arch by Eq. 1. The acceleration time-history curves of El wave (Input in X direction and Z direction) and WT wave (Input in X direction and Z direction) of model calculation used baseline correction. The peak acceleration of X direction input seismic wave was 0.4g, and the duration was 43.16 s and 70 s, respectively. The peak acceleration in Z direction input seismic wave was 0.45 times and 0.67 times in X direction for El wave and WT wave, respectively. In order to be consistent with the model test, the X direction and X-Z direction seismic waves were selected. The surrounding rock and primary lining adopted a solid elements, and the secondary lining used a plate elements. The surrounding rock material applied the Mohr-Coulomb strength failure criterion, and the primary support and secondary lining were elastic models. Boundary conditions used curved surface springs.

$$E = E_0 + S_g E_g / S_c \tag{1}$$

In the Eq. 1: E - Converted elastic modulus of concrete. E_0 - Elastic modulus of the original concrete. S_g - Cross-sectional area of steel arch. S_c - Cross-sectional area of concrete. E_g - Elastic modulus of steel arch.

Table 6. Physical and mechanical parameters of the model.

	γ / kN/m³	μ	c / kPa	φ / °	E / GPa
Surrounding rock	15	0.2	22.4	29.8	0.11
Primary lining	22.5	0.25	-	-	32
Secondary lining	23	0.2	-	-	30

5.2. Dynamic response of slope displacement and peak acceleration

The El wave and WT wave with a peak acceleration of 0.4 g were loaded on the slope without a tunnel and one-third of the tunnel slope, respectively. The loading directions were the X direction and X-Z direction, and the variation of slope displacement and peak acceleration was showed as Figure 15a–d, the displacement of the slope without a tunnel first increased, and then decreased. The PGDx of the slope surface was similar whether input wave in X-Z direction or in the X direction. It indicated that the peak value size of input seismic wave in Z direction was small to effect on the

Preprints (www.preprints.org) | NOT PEER-REVIEWED | Posted: 18 September 2023 doi:10.20944/preprints202309.1122.v1

response of the X direction when peak value of the input seismic wave in X direction was same. Compared with the slope without the tunnel, the tunnel had a significant inhibitory effect on the soil below it. It was indicated that the tunnel had obvious inhibitory effect on PGDx and PGAx of the ground below it with the comparing of PGD and PGA of the slope without tunnel and with tunnel portal at the one-third of the slope height. The PGD of the mark points of the middle section of the slope in the numerical simulation and the test was extracted for comparative analysis, indicating that the change law of numerical simulation were basically consistent with it of the tests (Figure 15b–d). PGDx-El-X: PGDx represented the PGD of the X direction, El represented input waveform, X represented input wave was in X direction. The label of the '*' represented the tests value.

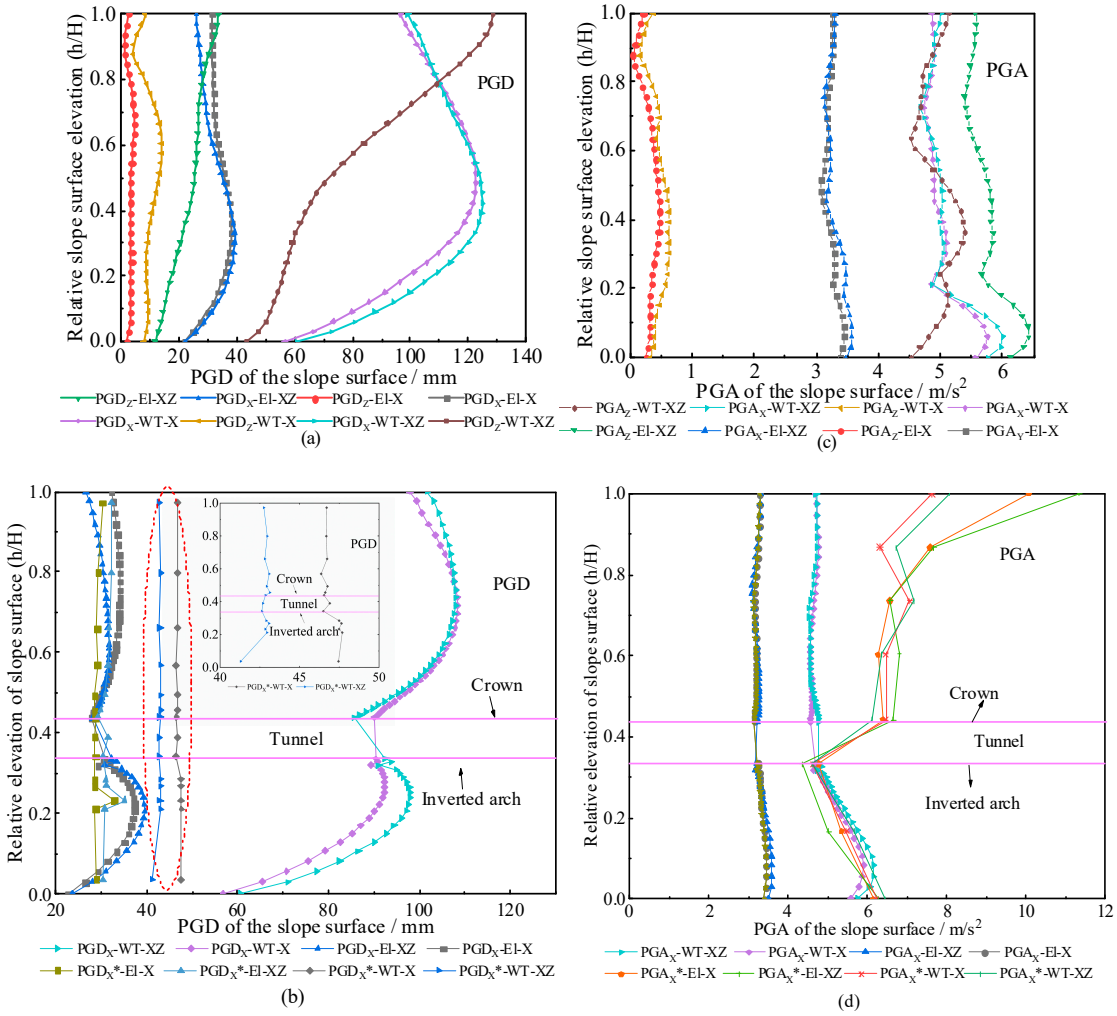

Figure 15. PGD and PGD variation of the slope surface with relative slope elevation. (**a**) The slope without tunnel, PGD; (**b**) Tunnel portal at one-third of the slope elevation, PGD; (**c**) The slope without tunnel, PGA; (**d**) Tunnel portal at the one-third of the slope elevation, PGA.

5.3. PGD and PGA of the tunnel variation with distance from tunnel portal

As shown in Figure 16a–d, under the X direction and X-Z direction loading conditions of the two waveforms, the PGDx and PGAx of the inverted arch and the vault basically appear at the portal position, and the displacement and peak acceleration of the inverted arch was slightly larger than that of the crown. It showed that the tunnel portal section was first damaged under horizontal shear action when the earthquake was strong.

Preprints (www.preprints.org) | NOT PEER-REVIEWED | Posted: 18 September 2023 doi:10.20944/preprints202309.1122.v1

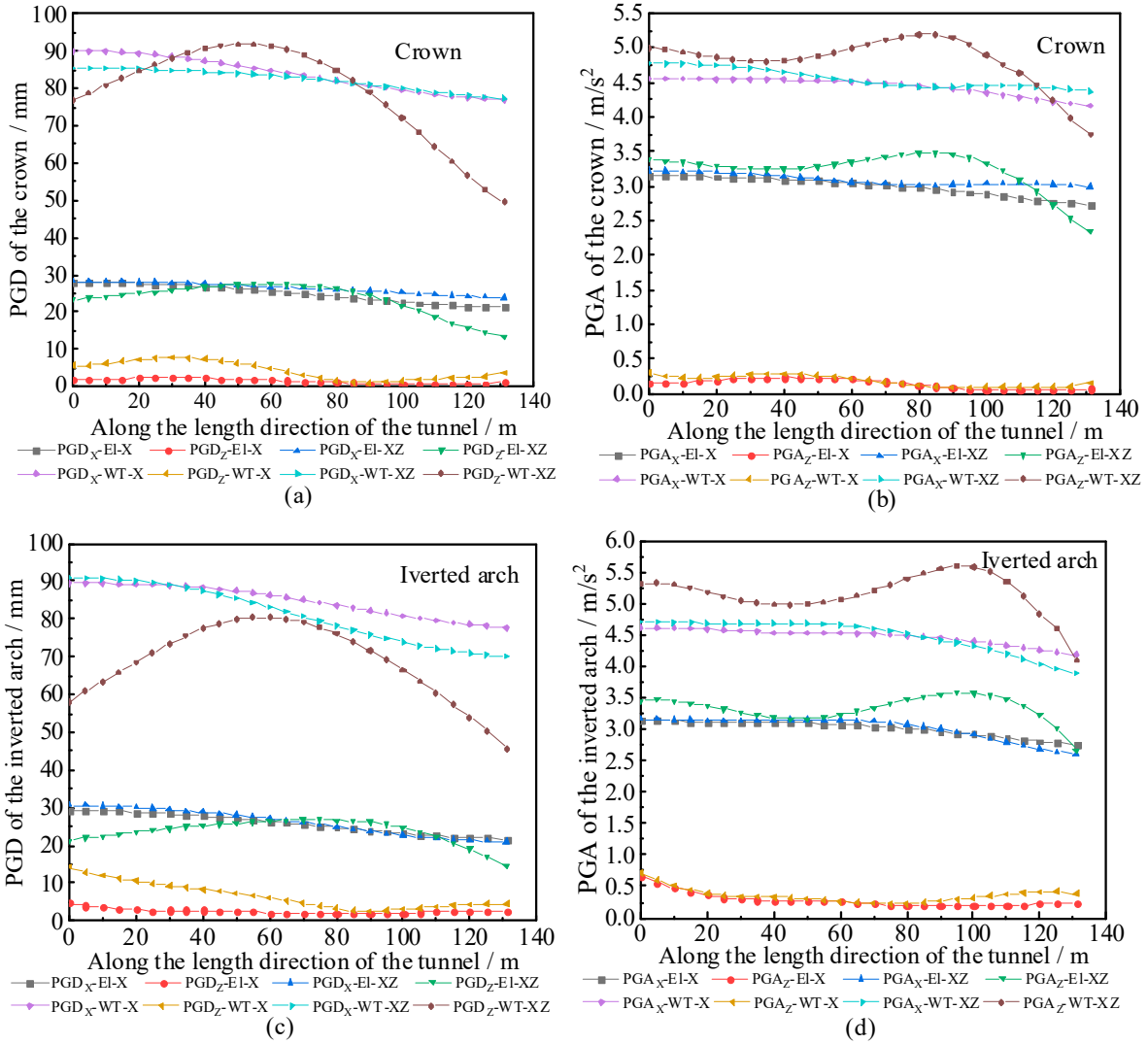

Figure 16. PGD and PGA variation of the crown and inverted arch with distance from tunnel portal. (**a**) The PGD variation of the crown with distance from tunnel portal; (**b**) The PGA variation of the crown with distance from tunnel portal; (**c**) The PGD variation of the inverted arch with distance from tunnel portal; (**d**) The PGA variation of the inverted arch with distance from tunnel portal.

6. Discussions

The dynamic response of a slope under seismic loading is very complex and influenced by various factors, among which displacement and acceleration are two critical indicators. Previous studies on pure slopes have shown that loess slope models experience a notable free-face amplification effect and vertical amplification effect on the input seismic wave [11,12]. On the slope surface and slope interior, the displacement and acceleration increase with the increasing of slope elevation, which shows an apparent elevation amplification effect [36,41]. Under the action of horizontal seismic waves, the dynamic response of the slope mainly appears in the middle and upper parts of the slope. An intense dynamic response primarily occurs in the middle and lower sections of the slope. The results of this paper indicated that the PGA and PGAAF of soil mass on the slope surface and within the slope beneath a tunnel is inhibited owing to the existence of the tunnel structure. The PGA and PGAAFs at the upper and lower interfaces of the tunnel structure also exhibit amplification effects, which is consistent with the numerical simulation results of Wang and Liang [42]. When the peak acceleration amplitude of the seismic wave is small, the existence of a tunnel has a specific reinforcement effect on the underlying ground and weakens the elevation amplification effect of acceleration. With the increasing of peak acceleration amplitude of the seismic waves, the

 doi:10.20944/preprints202309.1122.v1

tunnel structure exerts an amplifying effect on seismic waves, which led to the failure of the middle and upper slopes. The stability of the tunnel entrance slope under strong earthquakes was directly related to the safety of tunnel operation.

7. Conclusion

The distribution characteristics of slope surface displacement of tunnel entrance slope are analyzed under different ground motions based on shaking table model tests and numerical simulation. The slope displacement and acceleration various are investigated. The main conclusions are summarized as follows.

(1) The main deformation style of the slope was horizontal movement and settlement when the seismic wave input was in the X and X-Z directions, respectively. On average, the PGD_X was approximately 4.97 – 5.5 times and 4.91 – 5.22 times as large as the PGD_Z when the input WT wave and El wave was in the X direction, respectively. Whereas, the average PGD_X was approximately 4.42 – 5.78 times and 4.83 – 5.12 times as large as the average PGD_Z when the input WT wave and El wave was in the X-Z direction, respectively. Therefore, the horizontal deformation was the primary deformation, and the X direction seismic wave had a greater impact on the deformation of the slope. The tunnel entrance slope was destroyed under the action of a large horizontal seismic acceleration. Slope failure ahead of a tunnel can be divided into four stages, i.e. elastic deformation stage, plastic deformation accumulation stage, local failure stage, and block failure stage. Under loading condition of SN9, PGD_X mutation of the slope surface indicated the slope failure, and critical horizontal displacement was 48 mm.

(2) From the PGA distribution of slope with tunnel, it could be seen that under the action of different seismic waves, and the obvious amplification effect appeared at the top of the slope and near the empty surface. The existence of the tunnel had a great influence on the PGA and the PGAAF of the ground surrounding it. Especially, the inhibition effect on the soil mass below the tunnel was the most obvious. However, this inhibition effect gradually weakened with the increasing of seismic wave peak acceleration. Additionally, the deformation of the slope with tunnel during the earthquake could be identified according to either the PGD, PGAAF or PGA. Particularly, it could be obviously explained by using the PGD when the large deformation of the slope first occurred.

(3) The existence of the tunnel had a great influence on the PGA of the soil mass surrounding it. This was because the seismic waves encounter a tunnel surface with clear differences in the physical properties of the medium during their propagation in the slope body, thereby forming a strong reflection and refraction effect, and the amplitude changes significantly. The seismic waves were scattered and refracted near the tunnel, resulting in a complex superposition of waves and decreased amplitude.

(4) The results from the numerical simulations were basically consistent with the experimental results, it showed that when the earthquake was strong, the tunnel portal section was firstly damaged under horizontal shear actions.

Author Contributions: Conceptualization, Qingguo Liang; methodology, Jianping Yue, Qingguo Liang; funding acquisition and project administration, Qingguo Liang, Lili Wang, Weiyu Sun; software, Jianping Yue; supervision and validation, Qingguo Liang, Chuntan Fan; writing—original draft, Jianping Yue; resources, Qingguo Liang, Lili Wang; data curation, Qingguo Liang; writing—review and editing, Jianping Yue, Qingguo Liang, Shijiu Li. All authors have read and agreed to the published version of the manuscript.

Funding: This study was financially supported by the National Natural Science Foundation of China (No.51968041, No.41562013), China Postdoctoral Science Foundation (No.2021M693843), Foundation of A Hundred Youth Talents Training Program of Lanzhou Jiaotong University, 2022 Gansu Province Excellent Graduate Student 'Innovation Star' Project (No.2022CX-ZX-531), Natural Science Foundation of Gansu Province (No. 21JR7RA788), National Natural Science Foundation of China (No. 52208392).

Data Availability Statement: Publicly available datasets were analyzed in this study. This data can be found here: [link/accession number].

Conflicts of Interest: The authors declare that they have no known conflict of interest that could have appeared to influence the work reported in this paper.

References

1. Liu D.S. Loess and the environment. Beijing: China Ocean Press **1985**.
2. Deng J.; Wang L.M.; Zhang Z.Z.; Bing H. Microstructure characteristics and forming environment of late Quaternary Period loess in the Loess Plateau of China. *Environ. Earth Sci.* **2010**, *59*, 1807–1817. https://doi.org/10. 1007/s12665-009-0162-x
3. Chang W.B.; Wang P.; Wang H.J.; Chai S.F.; Yu Y.F.; Xu S.Y. Simulation of the Q^2 loess slope with seepage fissure failure and seismic response via discrete element method. *B. Eng. Geol. Environ.* **2021**, *80*, 3495–3511. https://doi.org/10.1007/s10064-021- 02139-z
4. Xu Y.R.; Allen M.B.; Zhang W.H.; He H.L. Landslide characteristics in the Loess Plateau, northern China. *Geomorphology* **2020**, *359*, 107150. https://doi.org/10.1016/j.geomorph.2020.107150.
5. Tao H.; Zhang M.M.; Gong L.; Shi X.; Wang Y.J.; Yang G.Q.; Lei S.W. The mechanism of slope instability due to rainfall-induced structural decay of earthquake-damaged loess. *Earthquake Research Advances* **2022**, *2*, 49–57. https://doi.org/10.1016/j.eqrea.2022.100 137
6. Wang J.D.; Li P.; Gu Q.; Xu Y.J.; Gu T.F. Changes in tensile strength and microstructure of loess due to vibration. *J. Asian Earth Sci.* **2018**, *169*, 298–307. https://doi.org/10.1016/j.jseaes. 2018. 10.011
7. Wang L.M.; Pu X.W.; Wu Z.J.; Xu S.H.; Liu K. Shaking table tests on dynamic response of loess slopes under coupling effects of earthquakes and rainfalls. *Chinese Journal of Geotechnical Engineering* **2018**, *40*, 1287–1293.
8. Xie D.Y.; Feng Z.Y. Consideration of some fundamental viewpoints in studying effective stress of unsaturated soils. *Chinese Journal of Geotechnical Engineering* **2006**, *28*, 170–173.
9. Tang H.M.; Jia H.B.; Hu X.L.; Li D.W.; Xiong C.R. Characteristics of landslides induced by the great Wenchuan earthquake. *J. Earth Sci-China.* **2010**, *21*, 104–113. https://doi.org/10.1007/s12583-010-0008-1
10. Wang L.M.; Wu Z.J.; Xia K.; Liu K.; Wang P.; Pu X.W.; Li L. Amplification of thickness and topography of loess deposit on seismic ground motion and its seismic design methods. *Soil Dyn. Earthq. Eng.* **2018**, *126*, 1–12. https://doi.org/10.1016/j.soildyn.2018. 02.021
11. Wu Z.J.; Zhang D.; Wang S.N.; Liang C.; Zhao D.Y. Dynamic response characteristics and deformation evolution of loess slopes under seismic loads. *Eng. Geol.* **2020**, *267*, 105507. https://doi.org/10.1016/j.enggeo.2020.105507
12. Wu Z.J.; Zhao D.Y.; Che A.L.; Chen D.W.; Liang C. Dynamic response characteristics and failure mode of slopes on the loess tableland using a shaking-table model test. *Landslides* **2020**, *17*, 1–5. https://doi.org/10.1007/s10346-020-01373-y
13. Pu X.W.; Wang L.M.; Wang P. Initiation mechanism of mudflow-like loess landslide induced by the combined effect of earthquakes and rainfall. *Nat. Hazards* **2021**, *105*, 3079–3097. https://doi.org/10.1007/s 11069-020-04442-6
14. Cheng X.S.; Zhou X.H.; Liu H.B.; Zhou Y.C.; Shi W. Numerical Analysis and Shaking Table Test of Seismic Response of Tunnel in a Loess Soil Considering Rainfall and Traffic Load. *Rock Mech. Rock Eng.* **2021**, *54*, 1005–1025. https://doi.org/10.1007/s006 03-020-02291-0
15. Sun W.Y.; Yan S.H.; Ma Q.G.; Liang Q.G.; Ou E.F.; Cao X.P.; Wang J.H.; Luo X.X. Dynamic response characteristics and failure mode of a bias loess tunnel using a shaking table model test. *Transp. Geotech.* **2021**, *31*, 100659. https://doi.org/10.1016/j.trogeo.2021. 100659
16. Liang Q.G.; Bian L.;, Zhang Q.P.; Huang J.; Wang M. Study on seismic dynamic characteristics of large section loess tunnel portal. *Journal of Highway and Transportation Research and Development* **2018**, *35*, 65–76.
17. Zhang J.D.; Liang Q.G.; Pu J.J.; Wang L.L.; Chai S.F. Experimental study on shaking table model of portal section of loess tunnel with different tunneling elevations. *Journal of Highway and Transportation Research and Development* **2018**, *35*, 77–85.
18. Bian L.; Liang Q.G.; Zhang Q.P. Experimental study on seismic responses of slope and portal of loess tunnel. *Railway Standard Design* **2018**, *62*, 79–84.
19. Fang J.; Liang Q.G.; Zhang Q.P.; He P., Wang L.L. Numerical simulation of dynamic responses of loess tunnel portal section with the consideration of tunneling elevation on the slope. *Earthquake Engineering and Engineering Dynamics* **2018**, *38*, 152–161.
20. Wang M.; Liang Q.G.; Wang L.L. Large-scale shaking table model study on dynamic response of loess tunnel side slope. *Earthquake Engineering and Engineering Dynamics* **2019**, *39*, 141–150.
21. Hashash Y.M.A.; Hook J.J.; Schmidt B.; Yao J.I-C. Seismic design and analysis of underground structures. *Tunn. Undergr. Sp. Tech.* **2001**, *16*, 247–293. https://doi.org/10.1016/s0886-7798 00051-7
22. Wang WL, Wang TT, Su JJ, Lin CH, Seng CR, Huang TH. Assessment of damage in mountain tunnels due to the Taiwan Chi-Chi Earthquake. *Tunn. Undergr. Sp. Tech.* **2001**, *16*, 133–150. https://doi.org/10.1016/s0886-779800047-5
23. Wang S.S.; Gao B.; Sui C.Y.; Wen Y.M. Shaking table test for seismic behavior of upward slope at tunnel entrance in different geological conditions. *Rock and Soil Mech.* **2014**, *35*, 278–284.
24. Gao B.; Wang S.S.; Wang Y.X.; Shen Y.S. Aseismic Study on Mountain Tunnels in High-Intensity Seismic Area. *Proceedings of the 2nd Czech-China Scientific Conference* **2016**. https://doi.org/10.5772/66805

25. Kazmi Z.A.; Extraction of Lagrangian Ground Displacements and Subsurface Seismic Stress Changes for Rational Earthquake Disaster Mitigation. Tokyo: University of Tokyo, 2013. https://doi.org/10.15083/000 06312
26. Yu H.T.; Chen J.T.; Yuan Y.; Zhao X. Seismic damage of mountain tunnels during the 5.12 Wenchuan earthquake. *J. Mt. Sci-Engl.* **2016**, *13*, 1958–1972. https://doi.org/10.1007/s11629-016-3878-6
27. Cui G.Y.; Wang M.N.; Lin G.J.; Wang W.J.; Zhang D. Statistical analysis of earthquake damage types of typical highway tunnel lining structure in Wenchuan seismic disastrous area. *Chinese Journal of Geological Hazard and Control* **2011**, *22*, 122–127.
28. Wang Z.Z.; Gao B.; Jiang Y.J.; Yuan S. Investigation and assessment on mountain tunnels and geotechnical damage after the Wenchuan earthquake. *Science in China (Series E: Technological Sciences)* **2009**, *52*, 546–558. https://doi.org/10.1007/s11431-009-0054-z
29. Asakura T.; Shiba Y.; Matsuoka S.; Oya T.; Yashiro K. Damage to Mountain Tunnels by Earthquake and Its Mechanism. *Doboku Gakkai Ronbunshu* **2000**, *659*, 27–38. https://doi.org/10.2208/jscej.2000.659_27
30. Niu J.Y.; Jiang X.L.; Wang F.F.; Yang H. Comparative Analysis of Dynamic Responses of Different Rock Tunnel Slopes. *Geotech. Geol. Eng.* **2019**, *38*, 1409–1430. https://doi.org/10.1007/s 10706 -019-01099-2
31. Bouckovalas G.D.; Papadimitriou A.G. Numerical evaluation of slope topography effects on seismic ground motion. *Soil Dyn. and Earthq. Eng.* **2005**, *25*, 547–558. https://doi.org/10.1016/j. soildyn.2004.11. 008
32. Carey J.M.; McSaveney M.J.; Petley D.N. Dynamic liquefaction of shear zones in intact loess during simulated earthquake loading. *Landslides* **2017**, *14*, 789–804. https://doi.org/10.1007/s10346-016-0746-y
33. Liu Y.R.; He Z.; Leng K.D.; Huang Y.Q.; Yang Q. Dynamic limit equilibrium analysis of sliding block for rock slope based on nonlinear FEM. *Journal of Central South University* **2013**, *20*, 2263–2274. https://doi.org/10.1007/s117 71-013-1733-2
34. Yang B.; Gao F.P.; Jeng D.S. Failure mode and dynamic response of a double-sided slope with high water content of soil. *J. Mt. Sci-Engl.* **2018**, *15*, 859–870. https://doi.org/10.1007/s11629-017-4616-4
35. Zhang Z.L.; Wang T.; Wu S.R.; Tang H.M.; Liang C.Y. Investigation of dormant landslides in earthquake conditions using a physical model. *Landslides* 2017,14, 1181-1193. https://doi.org/10.1007/s10346-017-0813-z
36. Lin M.L.; Wang K.L. Seismic slope behavior in a large-scale shaking table model test. *Eng. Geol.* **2006**, *86*, 118–133. https://doi.org/10.1016/j.enggeo.2006.02.011.
37. Yan Z.X.; Zhang S.; Zhang X.D.; Jiang P. Dynamic response law of loess slope with different shapes. *Adv. Mater. Sci. Eng.* **2019**, *2019*, 1–7. https://doi.org/10.1155/2019/4853102
38. Song D.Q.; Che A.L.; Zhu R.J.; Ge X.R. Dynamic response characteristics of a rock slope with discontinuous joints under the combined action of earthquakes and rapid water drawdown. *Landslides* **2017**, *15*, 1109–1125. https://doi.org/10.1007/s10346-017-0932-6
39. Wang K.L.; Lin M.L. Initiation and displacement of landslide induced by earthquake - a study of shaking table model slope test. *Eng. Geol.* **2011**, *122*, 106–114. https://doi.org/10.1016/j.enggeo.2011. 04.008.
40. Ye H.L.; Zheng Y.R.; Du X.L.; Li A.H. Shaking table model test and numerical analysis on dynamic failure characteristics of slope. *China Civil Engineering Journal* **2012**, *45*, 128–135.
41. Danneels G.; Bourdeau C.; Torgoev I.; Havenith H.B. Geophysical investigation and dynamic modelling of unstable slopes: case-study of Kainama (Kyrgyzstan). *Geophys. J. Int.* **2008**, *175*, 17–34. https://doi.org/10.1111/j.1365-246x.2008.03873.x
42. Wang L.L.; Liang Q.G.; Sun W.; Guan Y.Z. Influence of portal elevation on dynamic response characteristics of loess tunnel portal section. *China Earthquake Engineering Journal* **2017**, *39*, 853–858.